ZnO thick films for NO2 detection: effect of different nanostructures on the sensors' performances

(Article begins on next page)

25 November 2024

ZnO thick films for NO$_2$ detection: effect of different nanostructures on the sensors' performances

Daniele Ziegler[1,2], Andrea Marchisio[1,2], Paola Palmero[1,2], Diego Pugliese[1], Valentina Cauda[1], Jean-Marc Tulliani[1,2*]

[1]Politecnico di Torino, Department of Applied Science and Technology, Corso Duca degli Abruzzi 24, 10129 Torino, Italy

[2]INSTM R.U. PoliTO-LINCE Laboratory

*Corresponding author: Tel: +39-011-0904700; E-mail address: jeanmarc.tulliani@polito.it

Abstract

In this paper, the great sensitivity and selectivity to NO$_2$ detection at low temperature down to ppb-level of zinc oxide (ZnO) thick-film sensors are reported.

Sensor performances of ZnO films prepared by screen printing technique were evaluated comparing two different ZnO nano-powders in wurtzite crystal structure. Powders were synthetized by hydrothermal route (HT-ZnO) and by auto combustion sol-gel synthesis (AC-ZnO). After proper characterization of the nanopowders, the thick film sensors were fabricated by screen-printing technique onto α-alumina substrates equipped with Pt interdigitated electrodes, followed by a thermal treatment. The sensor response was studied in the range 50 – 250 °C. Best results were reached at 150 °C, with sensor response R (Z_g/Z_0) - defined as the ratio between impedance under NO$_2$ (Z_g) and impedance under dry air (Z_0) - equal to 42.92 for HT-ZnO and to 23.18 for AC-ZnO under 0.5 ppm of NO$_2$ in dry conditions. Finally, response and recovery time were measured, and selectivity of the sensors was determined by exposing the film toward O$_3$, CO$_2$, CH$_4$, N$_2$O and humidity at the best working temperature. Both sensors showed great sensitivity for NO$_2$ detection, supporting the exploitation of these sensors as NO$_2$ detectors at ppb level.

Keywords: Metal oxide semiconductor; Zinc oxide; Flower-like nanostructure; Hydrothermal synthesis; Combustion synthesis; Nitrogen dioxide detection.

1 Introduction

The major provenances of nitrogen oxides (NOx) anthropogenic emissions are the combustion processes in stationary and mobile sources [1]. In many ambient conditions, nitric oxide (NO) is emitted and quickly oxidized into nitrogen dioxide (NO_2) in the troposphere by atmospheric oxidants like O_3. Consequently, this is the main reaction for atmospheric NO_2 production, even if other contributions from specific non-combustion industrial processes like the manufacture of HNO_3, the utilization of explosives and welding have been considered [1].

Among NO_x, the most relevant pollutant against human health is NO_2. NO_2 gas is soluble in water, reddish-brown, and it is characterized by a typical pungent odor. NO_2 is an important atmospheric trace gas for several reasons, since it absorbs visible solar radiation and it generates impaired damaged visibility. Moreover, it has a potential direct function in global warming if its levels are high enough. Thus, it is one of the main gases controlling the oxidizing capability of the free troposphere by regulating the presence of radicals, such as $OH^\bullet$. Moreover, it displays a crucial role in determining O_3 levels in the troposphere since the NO_2 photolysis acts as initiator of the photochemical generation of O_3, either in polluted or unpolluted environments [2]. Finally, NOx play an essential role in the formation of ozone (O_3) and of secondary inorganic aerosols (SIA), through nitrates, increasing the amount of PM_{10} and $PM_{2.5}$ in the troposphere [3].

Dangerous effects for human health can result both from short-term exposure (e.g. deterioration of lung function) and long-term exposure (e.g. increased susceptibility to respiratory infection).

For instance, an epidemiological study [4] confirmed that high amounts of NO_2 were responsible for high levels of respiratory symptoms, exemplifying that NO_2 toxicity is dangerous for children.

For these reasons, for NO_2, the limit values are specified for 1 hour and annual exposures and EU Member States had to transpose them by January 1st, 2010. The 1-hour value can be exceeded up to 18 times per year before reaching the limit value, and the [NO_2] Threshold Limit Value (TLV) is equal to 106 ppb. The 2008 Air Quality Directive (EU, 2008c) also defined an alert threshold value of 213 ppb. In EU, the TLV annual mean [NO_2] concentration was set at 21 ppb.

Nowadays, wide spatial NO_x monitoring is restrained because of the limited availability of the monitoring equipments, such as continuous chemiluminescence monitors, that are characterized by high volumes and elevated prizes. Moreover, they require elaborated infrastructures, scientific and technical support and continuous power supply. In order to overcome the above-mentioned shortcomings, passive samplers have been successfully used for large scale monitoring of NO_x in the ambient environment [5].

In the detection of NO$_2$, metal oxide semiconductor (MOS) based gas sensors evidence an intriguing potential, compared to traditional measurement techniques, considering their low cost, ease of operation, high long-term reliability and stability as well as a moderate power dissipation [6].

In this respect, ZnO exhibits a great interest for its possibility to tune different features. In particular, nanostructures with different sizes and morphology can be easily prepared by various synthetic routes, obtaining ribbons, tubes, rods, wires, and tetrapods. ZnO is a semiconductor characterized by a stable wurtzite crystal structure, showing both piezoelectric and pyroelectric features. Thus, for its unique combination of different properties, it finds application in several fields such as transparent electronics, dye-sensitized solar cells, lithium-ion batteries, water splitting photoelectrochemical cells, ultraviolet (UV) light emitters and sensors, piezoelectric nanogenerators, chemical and temperature sensors, water remediation from organic pollutants, and spin electronics [7].

Crystalline ZnO exhibits thermochromic characteristics, varying the color from white to yellow when heated in air and reverting to white when it is cooled [8]. The hexagonal wurtzite structure is the most stable at ambient conditions, whereas the zinc blende phase can be stabilized by growing ZnO on substrates with cubic lattice structure. In both cases, Zn and O centers are tetrahedral. Finally, the rocksalt structure is only observed at relatively high pressures of about 10 GPa [9].

Although it occurs naturally as the mineral zincite, most ZnO is produced synthetically [10]. As a typical n-type semiconductor, it exhibits unique properties to work as an ideal gas sensor, like the wide band-gap (3.4 eV), large exciton binding energy of 60 meV, considerable electron mobility and photoelectric response, and excellent chemical and thermal stability [11–16].

A ZnO chemo-resistive sensor works often at 300–500 °C [17–19], since enough thermal energy of surface redox reaction is required to overcome the activation energy barrier improving the reaction kinetics [20]. However, the high temperature of operation adversely limits its wide application, because of the highest power required and increased potential risk of gas explosion [21]. The urgent task, therefore, is to decrease the operating temperature of ZnO based gas sensors, fabricating more portable and cost-effective devices, in accordance with the current developing trend [22]. For instance, Tesfamichael et al. [23] prepared W-doped ZnO thin films by magnetron sputtering. It was observed that the hybrid sensor showed significant higher sensing performance toward 5–10 ppm NO$_2$ at low operating temperature of 150 °C. In other works [24-26], ZnO nanostructures in the form of nanopetals, nanowalls and composites were presented as room-temperature NO$_2$ sensors. Though a very high sensor response as well as fast response and recovery times were achieved in ref. [24], only one NO$_2$ concentration was investigated (20 ppm), thus no information on the limit of detection was available. On the contrary, in ref. [25], several

concentrations were studied (5-50 ppm) but the sensor response was about 30 times lower under 20 ppm NO_2, compared to the work [24]. Finally, in [26], the sensors were tested down to 1 ppm of NO_2. However, in [25, 26], none of the prepared sensors reached a stable response when exposed to gas, even after 15 min [26].

For these reasons, in this work, in order to develop sensitive ZnO thick films for NO_2 detection below 1 ppm at low temperature, two synthesis routes were carried out. In the first one, ZnO nanoparticles were obtained by a sol-gel auto-combustion synthesis, while in the second one, a hydrothermal route was accomplished for synthetizing ZnO flower-like nano-powder. Sensors were fully characterized, and the sensors optimum operating temperature was determined. At this temperature, sensors performances were studied in terms of sensitivity, selectivity and response/recovery times.

2   Experimental
2.1   Powder synthesis

ZnO powders were synthesized by two different routes: auto-combustion and hydrothermal syntheses.

In the first synthesis, zinc nitrate hexahydrate ($Zn(NO_3)_2 \cdot 6H_2O$, Sigma Aldrich, 99.9%) and soluble potato starch (($C_6H_{10}O_5)_n$, Sigma Aldrich) were used without any further purification.
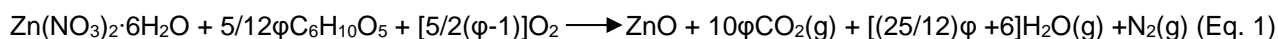
Starches from different botanical sources vary widely in structure and composition, but all granules consist of two major molecular components, i.e. amylose and amylopectin, both polymers of α-glucose units in the 4C1 conformation. In amylose, these units are linked (1→4), with the ring oxygen atoms all on the same side, whereas in amylopectin some residue in every twenty is also linked (1→6) forming branch-points.

Two solutions were prepared, the first containing 0.04 mole of $Zn(NO_3)_2 \cdot 6H_2O$ dissolved in 100 mL of deionized water, the second with 0.42 mole of potato starch in the same amount of water. Potato starch solution was heated at 80 °C and maintained under vigorous magnetic stirring for 1 h to ensure a proper dissolution. After adding zinc nitrate to starch solution, the mixture was further stirred for 15 min in an Al_2O_3 crucible. The resultant mix was turbid, due to a partial starch gelling during mixing. The crucible was then placed in a water bath at 90 °C and kept under continuous stirring for 5 h, providing a viscous and dense white-yellowish gel. Thereafter, the crucible was heated at 300 °C for 30 min (heating rate of 10 °C/min) to provide ignition of reagents, whose combustion was accomplished in about 1 min. The product was a spongy brown friable mix of ZnO, partially unreacted reagents and carbon as confirmed by TGA analysis, as reported later.

After manual grinding, the powder was calcined at 500 °C for 2 h (heating rate of 10°C/min). The resultant product was a bright white fine powder, which was further submitted to manual grinding.

This novel synthesis route exhibits a yield of 90%. The amount of reactants and their relative proportions were selected according to the reaction stoichiometry. The proportion fuel/oxidant (φ), i.e. potato starch/nitrate, was equal to 2.25. In this case, a highly rich mixture with a significant lack of oxidant was used. In these conditions, the amount of the oxidant is not enough to ensure the complete oxidation of the starch, acting as a fuel. As a result, additional oxygen from the air is required, but in the synthesis conditions this additional amount is not provided properly. This results in a partial pyrolysis of the fuel, instead of the complete oxidation [27-29].

For the value of the parameter φ, the Eq. (1), derived according to the principles of the combustion processes [27-29], describes the overall process:

$$Zn(NO_3)_2 \cdot 6H_2O + 5/12\varphi C_6H_{10}O_5 + [5/2(\varphi-1)]O_2 \longrightarrow ZnO + 10\varphi CO_2(g) + [(25/12)\varphi + 6]H_2O(g) + N_2(g) \quad \text{(Eq. 1)}$$

In accordance with Eq. 1, the whole reaction causes the production of a large amount of gaseous products. Carbonaceous materials are formed during the process and these create a matrix where ZnO particles and unreacted reagents are trapped. This and the large amount of gases generated avoid aggregation and sintering of ZnO particles during the synthesis. Moreover, the carbonaceous matrix is burned during heating of the intermediate products at 500 °C for 1 h. In these conditions, another abundant production of gases is induced, supposing the complete oxidation of the carbonaceous material to produce CO_2 and H_2O.

The ZnO desert-rose nanoparticles were synthesized by a hydrothermal method, as previously reported in detail [30].

In the hydrothermal synthesis, all the reagents were used without any further purification. In a typical synthesis, 0.05 mole of potassium hydroxide (KOH, 1 M, Merck) and 0.25 mole of zinc nitrate hexahydrate ($ZnNO_3 \cdot 6H_2O$, 0.5 M, from Sigma-Aldrich) were dissolved separately in 50 mL of bi-distilled water (from Direct-Q system, Millipore). Then, the zinc nitrate solution was dropped slowly into KOH under vigorous stirring in a total volume of 100 mL, resulting in the formation of a white gel. The obtained white gel was subsequently transferred in a closed Teflon vessel and kept at 70 °C for 4 h. Finally, the precipitated ZnO powder was carefully separated from the solution by filtration, washed many times with deionized water to neutralize the pH value and finally dried at 60 °C overnight in air. ZnO white nano-powder was obtained after annealing at 450 °C for 2 h (HT-ZnO).

2.2 Powder and film characterization

The particle size distribution of AC-ZnO and HT-ZnO powders was determined by laser granulometry (Mastersizer 3000, Malvern, UK). The powders were manually ground in an agate mortar and dispersed for 5 min in absolute ethanol under ultrasonication prior to the analysis.

Differential thermal analysis-thermogravimetric analysis (DTA-TG, STA 409, Netzsch, Selb, Germany) was performed on HT-ZnO precursor in the temperature range 25-900 °C with a heating ramp of 10 °C/min under static air.

The crystalline structure of the synthetized powders was assessed through the X-Ray diffraction (XRD) technique. Spectra were recorded on a Pan'Analytical X'Pert Pro instrument (Pan'Analytical, Almelo, The Netherlands) with Cu K_α radiation (0.154056 nm) in the 2θ range between 10 and 70°, working with a 2θ step size of 0.0065° and an acquisition time per step of 23 s. Diffraction patterns were indexed with the Powder Data File database (P.D.F. 2000, International Centre of Diffraction Data, Newtown Square, PA, USA).

The average crystallite size was estimated according to the Scherrer's equation (Eq. 2):

$$D = k\lambda / \beta\cos\theta \qquad \text{(Eq. 2)}$$

where k is a constant assumed to be equal to 0.9, λ is the Cu K_α wavelength (0.154056 nm), θ is the half of Bragg (radiants) and β is the full width at half maximum of the X-ray diffraction peaks.

The Brunauer−Emmett−Teller (BET) specific surface area (SSA) of the AC-ZnO and HT-ZnO nanoparticles was measured from N_2 sorption isotherms (Quadrasorb SI, Quantachrome) by multipoint method within the relative pressure range of 0.1−0.3 P/P_0. The pore size distribution of the particles was estimated from the desorption branch using the Density Functional Theory (DFT) model.

The morphology of both AC-ZnO and HT-ZnO powders and sensors was investigated by means of Field Emission-Scanning Electron Microscopy (FE-SEM, Dual Beam Auriga from Carl Zeiss, operating at 5 keV). A thin Cr film was sputtered onto the samples prior to the observations.

2.3 Realization of gas sensors

Sensors were fabricated by screen-printing technique onto α-alumina substrates (Coors Tek, USA; ADS-96: 96% alumina, 0.85 cm × 1.7 cm) with Pt interdigitated electrodes (ESL 5545, USA). The Pt ink was fired at 980 °C for 18 min after screen-printing deposition to obtain a high-grade adhesion and optimize its electrical conductivity. Electrodes present a thickness of 400 µm and are

spaced 450 μm one from each other. Moreover, the edge of an electrode of one comb and the vertical connection of the second comb are separated by 400 μm. The ink for screen-printing deposition was realized by mixing the ZnO powder with an organic vehicle (ethylene glycol monobutyral ether, Emflow, Emca Remex, USA), to achieve the proper rheological characteristics, and polyvinyl butyral (PVB), acting as temporary binder for the powder before firing. After screen-printing deposition with a 325-mesh steel mask, the sensors were dried at room temperature overnight and fired at 500 °C in air for 1 h (2 °C/min heating and cooling rates). This process is mandatory to remove organic residues and to guarantee an optimal adhesion with the substrate.

After fabrication, sensors were tested in a home-made system [31]. All tests were performed under 1000 standard cubic centimeters (SCCM). Target gas from certified bottle (SIAD, Bergamo, Italy) was diluted in dry air by means of flow meters (Teledyne Hastings Instruments HFM 300 controller and flow meters HFC 302, Teledyne Hastings, Hampton, VA, USA). Sensors were heated by a Ni-Cr wire, located underneath the sensor, with a DC power supply (Peak Tech, Nanjing, Jiangsu, China). A PT1000 resistance temperature detector (RS Pro, London, UK) was used for temperature calibration.

Since selectivity of semiconductor gas sensors is a key requirement, different cross-sensitivity tests were performed at the optimum working temperature of 150 °C. For this reason, variations in film impedance were recorded after exposure for 10 min to different target gases comparing the sensor's impedance under pure air over the same amount of time. Sensor responses with respect to CH_4 100 ppm, CO_2 500 ppm, O_3 200 ppb, RH 50% (at room temperature), N_2O 15 ppm and NH_3 50 ppm were determined.

O_3 was generated by a UV lamp (SOG-01, UVP-LLC Cambridge, UK) from a constant air flow of 1000 SCCM of compressed air. The modulation of the O_3 amount was carried out by changing the length of lamp exposed and was determined with calibration curves provided by the manufacturer.

NO_2 and O_3 losses due to adsorption and reactions in pipelines and measuring chamber were prevented by adopting polymers such as polytetrafluoroethylene (PTFE) and polyvinylidene fluoride (PVDF) tubes.

During sensor tests, film impedance was measured with a LCR meter (Hioki 3533-01, Nagano, Japan). Impedance's measurements were carried out by means of a constant AC tension of 1 V and a frequency of 1 kHz, and sensors were located into a chamber of 0.1 L volume.

The response of the sensor (R) was defined in accordance to the Eq. (3) for oxidizing gases and to the Eq. (4) for reducing species:

$$R = Z_g/Z_0 \text{ (Eq. 3)}$$

$$R = Z_0/Z_g \text{ (Eq. 4),}$$

where Z_g and Z_0 are the impedance under target gas and the impedance under dry air, respectively, of the ZnO layer at the equilibrium.

The response time (i.e. the time required by a sensor to achieve 90% of the total impedance change in the gas adsorption) as well as the recovery times (i.e. the time needed for a sensor to reach 90% of the total impedance variation in the case of gas desorption) were also determined in the present work.

AC-ZnO and HT-ZnO sensors were firstly tested toward NO_2 0.25 ppm in dry conditions at different temperatures (from 50 °C to 250 °C in steps of 50 degrees), evaluating the best working temperature. Sensors' performances under different NO_2 levels, namely 50, 100, 200 and 500 ppb, were investigated at the optimum temperature, and the obtained results were compared with those of analogous works using ZnO for NO_2 monitoring at low temperature.

Dynamic tests were performed, and after the film had reached the equilibrium in dry air (baseline impedance), NO_2 was introduced into the sensor chamber until a new equilibrium on the sensor surface was achieved. Then, NO_2 was switched off and the sensor was exposed to dry air until a novel equilibrium between the film surface and the adsorbed species was reached.

3 Results and discussion

3.1 Powder and film characterization

The particle size distributions of as-synthesized AC-ZnO and HT-ZnO powders are depicted in Fig. 1, together with a comparison of their cumulative curves. AC-ZnO exhibits a trimodal distribution, with maxima at 0.4, 2.9 and 11.9 µm. This powder shows a higher degree of agglomeration compared to the quasi-monomodal distribution of HT-ZnO with maximum located at 3.3 µm. Table 1 collects the d10, d50 and d90 values (i.e., the particle size corresponding to 10%, 50% and 90% of the volume cumulative distribution) for both powders, still showing the finer and narrower distribution of HT-ZnO as compared to AC-ZnO.
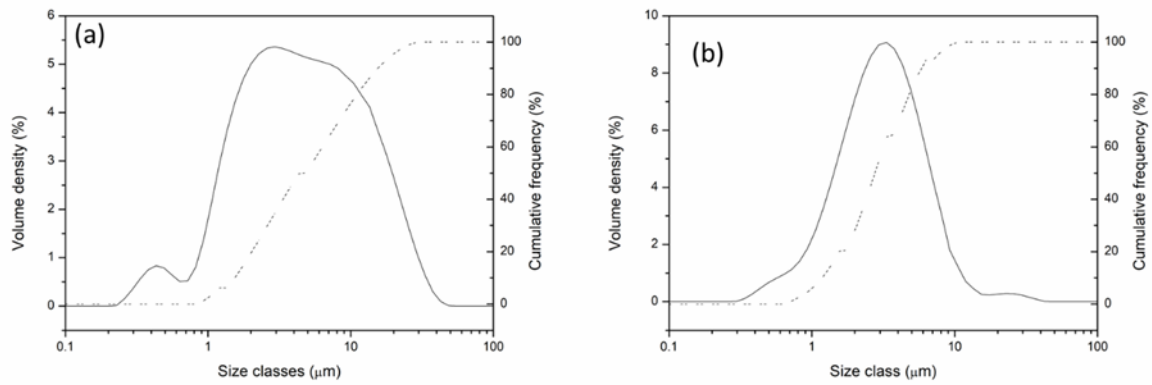
Fig. 1 ZnO particle size distribution of AC-ZnO (a) and HT-ZnO (b) in volume density % (straight line) and as cumulative frequency % (dashed line).

Table 1 Particle size corresponding to 10% (d10), 50% (d50) and 90% (d90) of the cumulative distribution for AC-ZnO and HT-ZnO

Cumulative %	AC-ZnO (µm)	HT-ZnO (µm)
d10	1.26	1.22
d50	4.40	3.06
d90	16.20	6.96

DTA-TG curves related to AC-ZnO powder pre-calcined at 300 °C for 30 min are shown in Fig. 2.
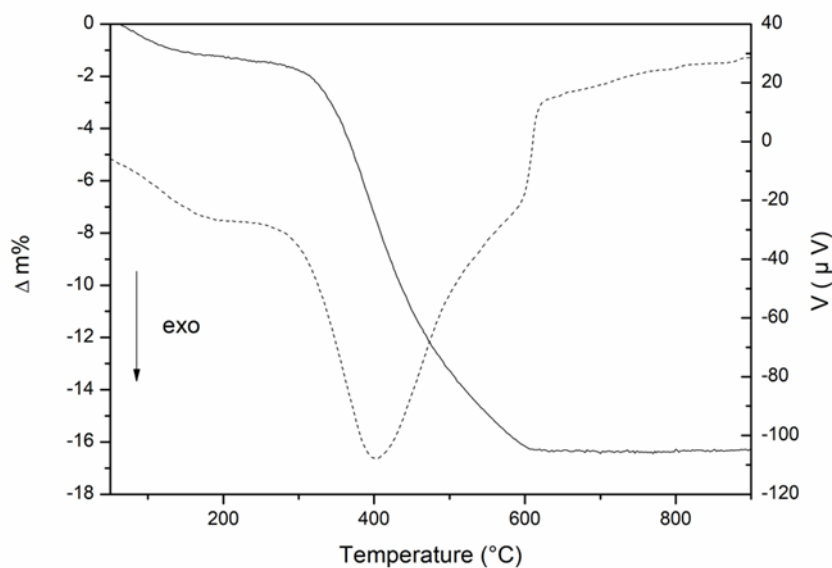
Fig. 2 TG-DTA curves in dynamic mode of AC-ZnO powder heated at 300 °C for 30 min with a 10 °C/min heating ramp (static air): TG continuous line, DTA dashed line

The TG curve exhibits a significant weight loss of 16.27%, starting from about 300 °C and almost accomplished at 600 °C.

The TG and DTA traces show three main regions. The first one at T < 300 °C is due to the decomposition of chemically bound groups of starch and the formation of the pyrochlore phases, as confirmed by XRD investigation (data not shown). This region is characterized by a slight mass loss (of about 1.8%). The second region from 300 to 600 °C is related to the decomposition of the pyrochlore phases and the formation of ZnO pure phases, as confirmed by XRD analysis carried out on powders thermally treated at 500 °C for 2 h (see Fig. 4). No weight loss between 600 and 900 °C was detected on the TG curve, confirming the formation of stable nanocrystalline ZnO as the decomposition product [32].

The X-Ray diffraction patterns of HT-ZnO, annealed at 450 °C for 2 h, and AC-ZnO, fired at 500 °C for 2 h, are reported in Fig. 3. Different heat treatment temperatures were selected to induce ZnO crystallization in each powder deriving from the various synthesis routes.
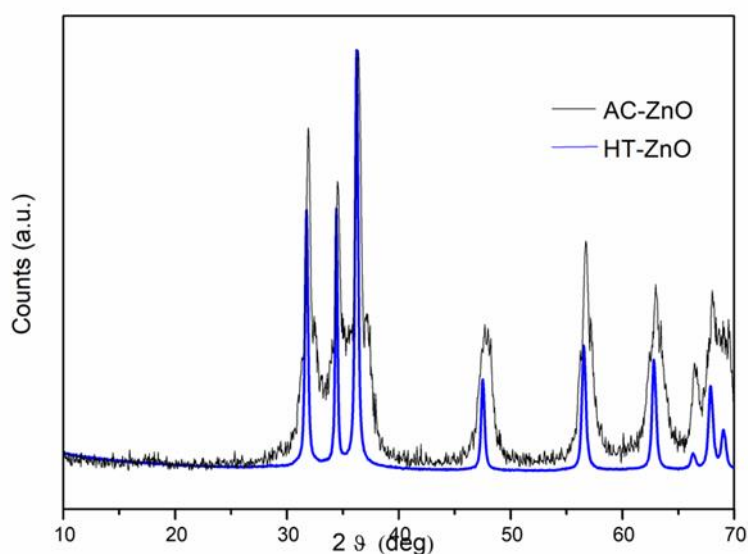
Fig. 3 XRD patterns of the HT-ZnO (blue line) and AC-ZnO (black line)

In the case of HT-ZnO, a well crystallized product, made of pure ZnO in hexagonal wurtzite structure (JCPDS file, No. 80-0074), was observed. By means of Scherrer's equation applied to (100), (002), (101), (102), (110) and (103) peaks, a crystallite size value of 38.6 ± 2.1 nm was obtained.

In the case of AC-ZnO, after annealing at 500 °C for 2 h, crystallization of the same hexagonal wurtzite structure was observed, even though with a lower degree of crystallization and with significantly smaller crystallites (14.8 ± 1.7 nm) considering the same six diffraction peaks.

The decrease in crystallite size for AC-ZnO compared to HT-ZnO powders can be related to the different synthesis route, since the annealing was carried out even at higher temperature for AC-ZnO compared to HT-ZnO (i.e. 500 °C for AC-ZnO and 450 °C for HT-ZnO). In fact, in the case of auto-combustion synthesis, the carbonaceous materials from starch create a matrix where ZnO particles and unreacted reagents are trapped. This phenomenon prevents aggregation and sintering of ZnO particles during this stage of the synthesis [33, 34].

The SSA, as measured by N_2 adsorption, revealed to be equal to 15.4 and 19.6 m^2/g for AC-ZnO and HT-ZnO, respectively, with corresponding average pore sizes of about 1 and 4 nm. Both values are in line with the one measured for nano-porous ZnO electrodes annealed at 400 °C for 5 min and sensitized with a ruthenium bipyridyl complex dye [35]. For instance, also in [36] higher SSA was obtained by hydrothermal route compared to sol-gel method.

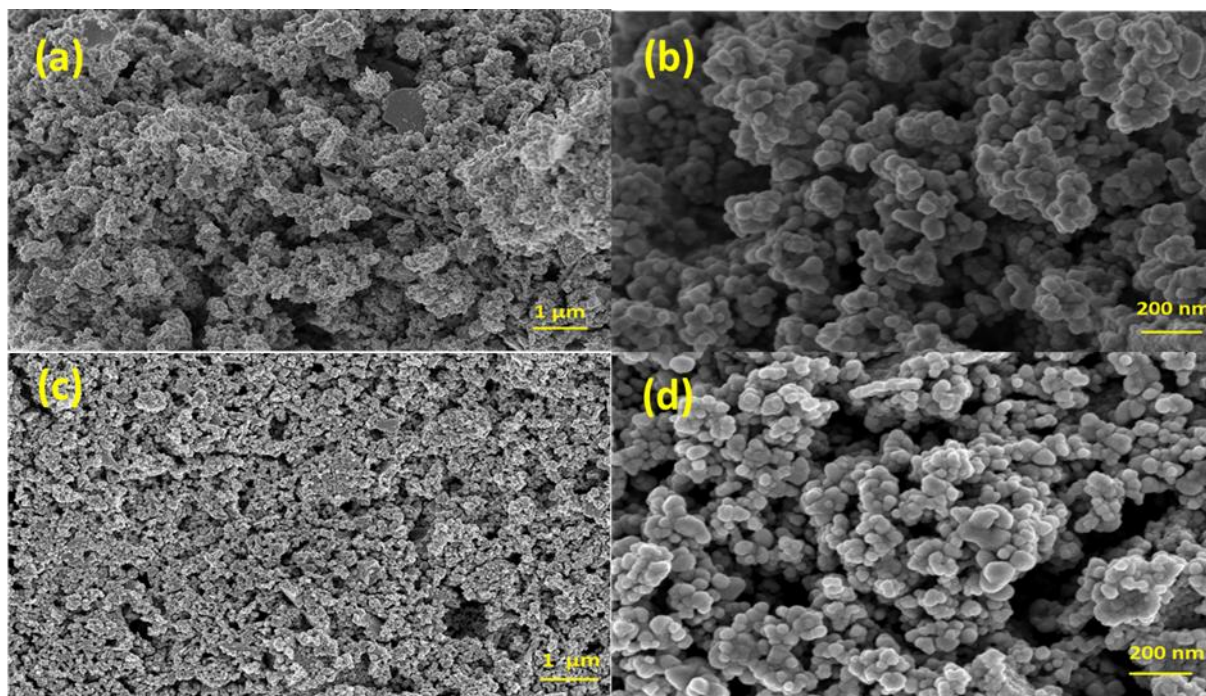The FE-SEM images of the AC-ZnO powder and film are depicted in Fig. 4.

Fig. 4 FE-SEM micrographs of: AC-ZnO powder (annealed at 500 °C for 2 h) at low (25 kx, a) and high (150 kx, b) magnification; AC-ZnO sensor (fired at 500 °C for 1 h) at low (25 kx, c) and high (150 kx, d) magnification

Fig. 4a shows that AC-ZnO powder is organized in a fluffy and spongy structure, rich of micro and nanopores and voids. The higher magnification image reported in Fig. 4b reveals that such porous structure is composed of agglomerates of nanosized particles (less than 50 nm in diameter). It is reasonable to assume that the carbon matrix formation during the first stage of the synthesis and its combustion during the final heat treatment contributed to obtain a final product, whereas the gases burn-out during auto-combustion were responsible for the formation of a highly porous structure [27, 28]. Furthermore, neither variations in the morphology after screen-printing deposition nor evidence of grain growth after firing the sensor at 500 °C for 1 h were observed compared to the powder obtained after 2 h of calcination at 500 °C. In fact, the morphology of the film is very close to that of the starting powder (Fig. 4c and d). Sensor thickness was measured in cross-section and a value of 18.7 ± 1.8 µm was attained as an average of 10 measurements.

In Fig. 5, the FE-SEM micrographs of the HT-ZnO powder and thick film after firing at 500 °C for 1 h are depicted.
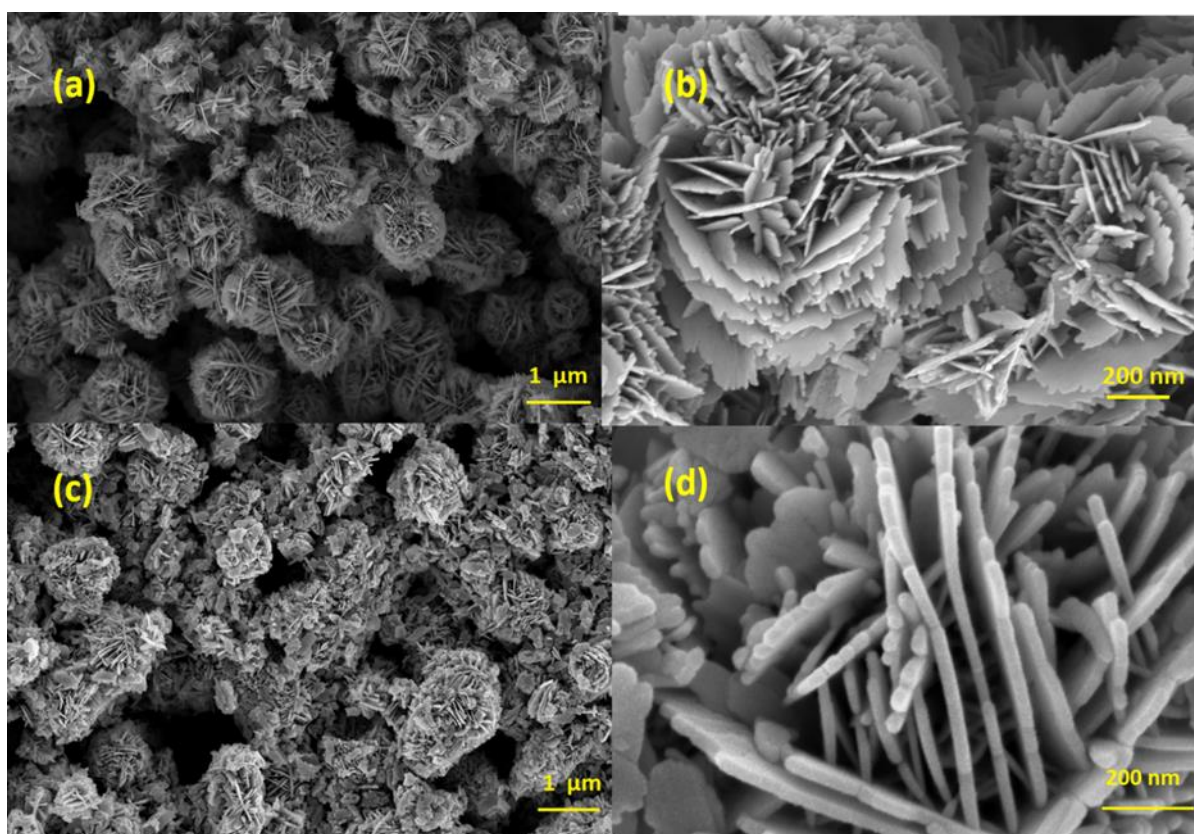
Fig. 5 FE-SEM micrographs of HT-ZnO powder (annealed at 450 °C for 2 h) at low (25 kx, a) and high (80 kx, b) magnification. Images of HT-ZnO sensor (fired at 500 °C for 1 h) at low (25 kx, c) and high (200 kx, d) magnification

The HT-ZnO powder and thick film reveal a flower-like-desert rose morphology of the particles. ZnO powder is composed of nearly spherical granules made of regular nanostructured prism-shaped planes as building blocks [35]. The ZnO agglomerates are composed of several flower-like primary nanoparticles, which consist of platelets of around 2 µm in diameter and thickness of around 10-20 nm [37].

The branched and nanostructured morphology of ZnO was completely maintained after the preparation of the sensor, and specifically the steps including screen-printing and firing at 500 °C for 1 h. In fact, the film showed the presence of the same granules, with petals' width of about 20 nm and rose-diameter of about 2-3 µm. In accordance with laser granulometry, in this case an extremely regular 3D development of nanoparticles and agglomerates was obtained. A sensors' thickness of 19.9 ± 2.1 µm was measured in FE-SEM cross section as an average of 10 measurements.

3.2   Gas sensing properties

Sensors were fabricated by screen-printing technique, as previously described, and after 500 °C firing for 1 h, a satisfying adhesion of the film over the α-alumina substrate was achieved and confirmed by scotch-tape test.

Fig. 6 shows the sensor response R (Z_g/Z_0) under 250 ppb NO_2 in dry air, at different operating temperatures, of the AC-ZnO and HT-ZnO sensors.
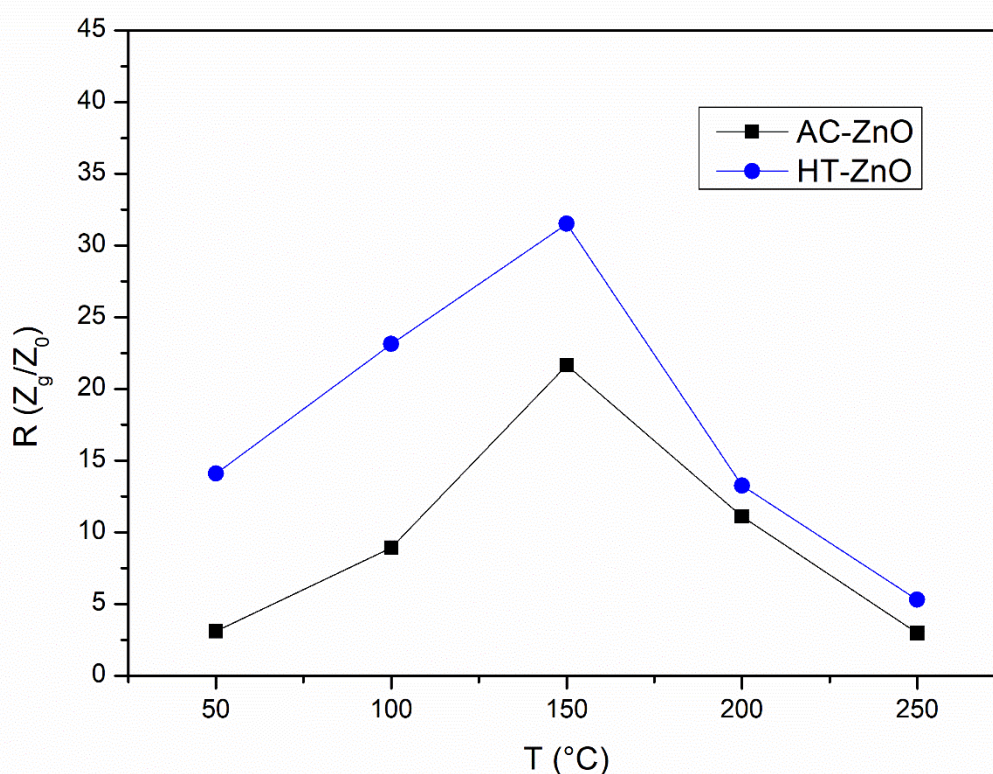

Fig. 6 Sensor film's response at different operating temperatures (in the range 50-250 °C) under 250 ppb NO_2 in dry air

At 150 °C, the impedance of the AC-ZnO film under dry air is equal to 990 kΩ and it reaches 21.46 MΩ under 250 ppb of NO_2. The HT-ZnO sensor's impedance increases from 840 kΩ in dry air up to 26.47 MΩ under the same concentration of nitrogen dioxide. Table 2 summarizes the sensor's response and response/recovery times at different temperatures of the AC-ZnO and HT-ZnO sensors.

Table 2 Sensor's response and response and recovery times at different temperatures under dry air and 250 ppb of NO_2 for AC-ZnO and HT-ZnO sensors

Temperature [°C]	R (AC-ZnO)	R (HT-ZnO)	Response time AC-ZnO [s]	Response time HT-ZnO [s]	Recovery time AC-ZnO [s]	Recovery time HT-ZnO [s]
50	3.11	14.09	1,502	404	12,034	5,099
100	8.91	23.14	1,098	361	3,207	2,122
150	21.67	31.51	652	341	788	451
200	11.10	13.26	609	236	105	273
250	2.96	5.30	289	160	24	106

The ZnO sensors behave as n-type semiconductors in the entire investigated temperature range: the gas sensors' impedance increases with the increase of the oxidizing target gas concentration. Considering the sensor response R (Z_g/Z_0), it reaches a maximum at 150 °C with the typical gaussian trend for both sensors (see Fig. 6). In all cases, recovery times decrease when increasing the operating temperature, as expected. Furthermore, the kinetics of adsorption follows a comparable trend. Impedance variations upon different nitrogen dioxide concentrations (in the range 50-500 ppb) at 150 °C are displayed in Fig. 7.
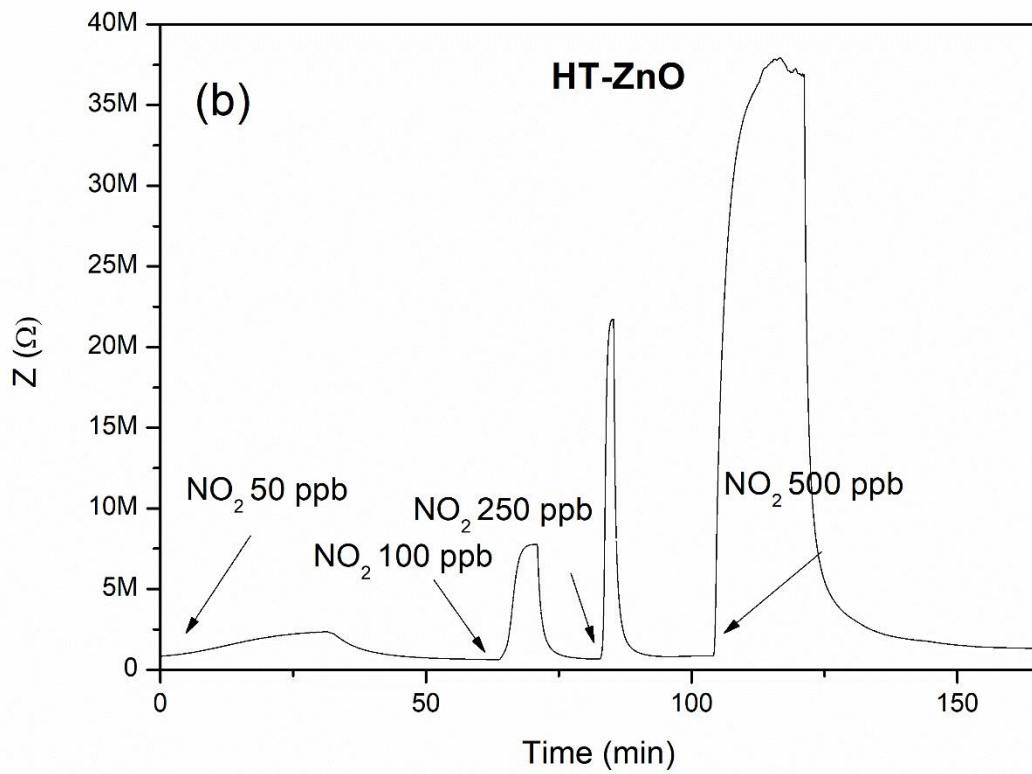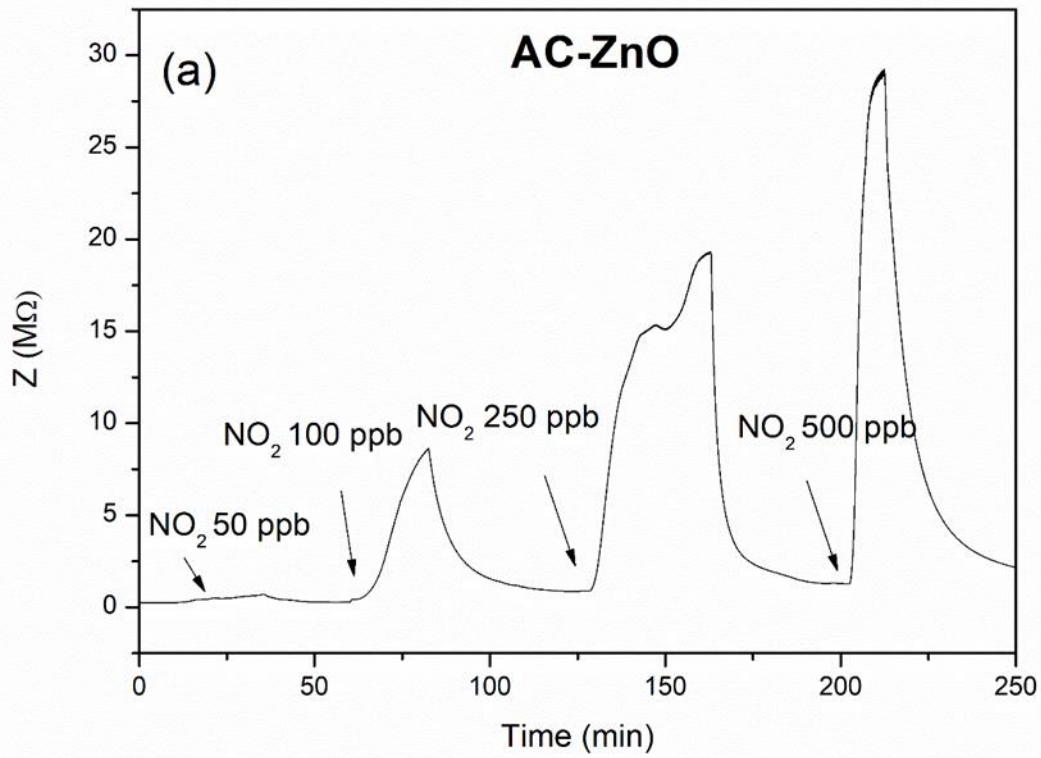
Fig. 7 Impedance's variations of (a) AC-ZnO sensor and (b) HT-ZnO sensor upon different NO_2 concentrations exposure at 150 °C.

The calibration curves of the proposed sensors are presented in Fig. 8. Comparing the sensors' performance under 500 ppb of NO_2 in dry conditions (see Fig. 8), HT-ZnO shows an almost doubled sensor response as compared to AC-ZnO (42.92 and 23.18, respectively). At the same time, the response and recovery times of HT-ZnO (341 and 451 s, respectively) are shorter than those of AC-ZnO sensor (652 and 788 s, respectively). This could be due to the higher surface area (19.6 vs 15.4 m^2/g) and to the lower degree of agglomeration of the flower-like ZnO hydrothermally prepared, as attested by laser granulometry and FE-SEM investigations. Moreover, in accordance with Korotcenkov et al. [38], the rate of sensor response toward oxidant species like O_3 and NO_2 increases by increasing the pore size. In fact, from N_2 adsorption measurement, the average pore size was 4 times higher for HT-ZnO than for AC-ZnO.
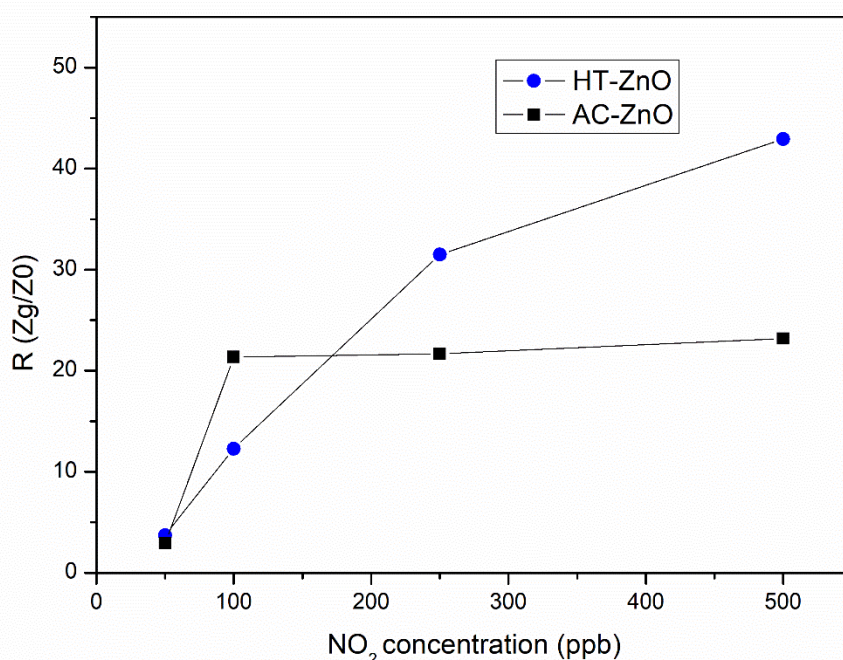

Fig. 8 Calibration curves of AC-ZnO (black) and HT-ZnO (blue) sensors.

AC-ZnO exhibits a sigmoidal trend in the investigated concentration range, with a quasi-saturation for concentrations higher than 100 ppb, whereas the HT-ZnO shows an increase in the sensor response when increasing the NO_2 amount from 50 up to 500 ppb following a quasi-linear trend in the form y = a + bc. A sensitivity of 0.094 ppb^{-1} (R^2 = 0.956) was calculated for the HT-ZnO sensor according to the IUPAC definition [39], which states that in the case of linear correlation the

sensitivity of the sensor can be determined from the slope of the interpolation line R = f([NO$_2$]). The sensor devices have been then tested for prolonged times after 3 months of storage and no differences in their performances has been noted, proofing the good thermo-mechanical and electrical stability of the sensing layers. Results of cross-sensitivity test carried out at 150 °C are reported in Fig. 9. Sensor responses of HT-ZnO and AC-ZnO sensors toward CH$_4$ 100 ppm, CO$_2$ 500 ppm, O$_3$ 200 ppb, RH 50% (at room temperature), N$_2$O 15 ppm and NH$_3$ 50 ppm were determined at 150 °C and compared with those upon NO$_2$ 250 ppb.
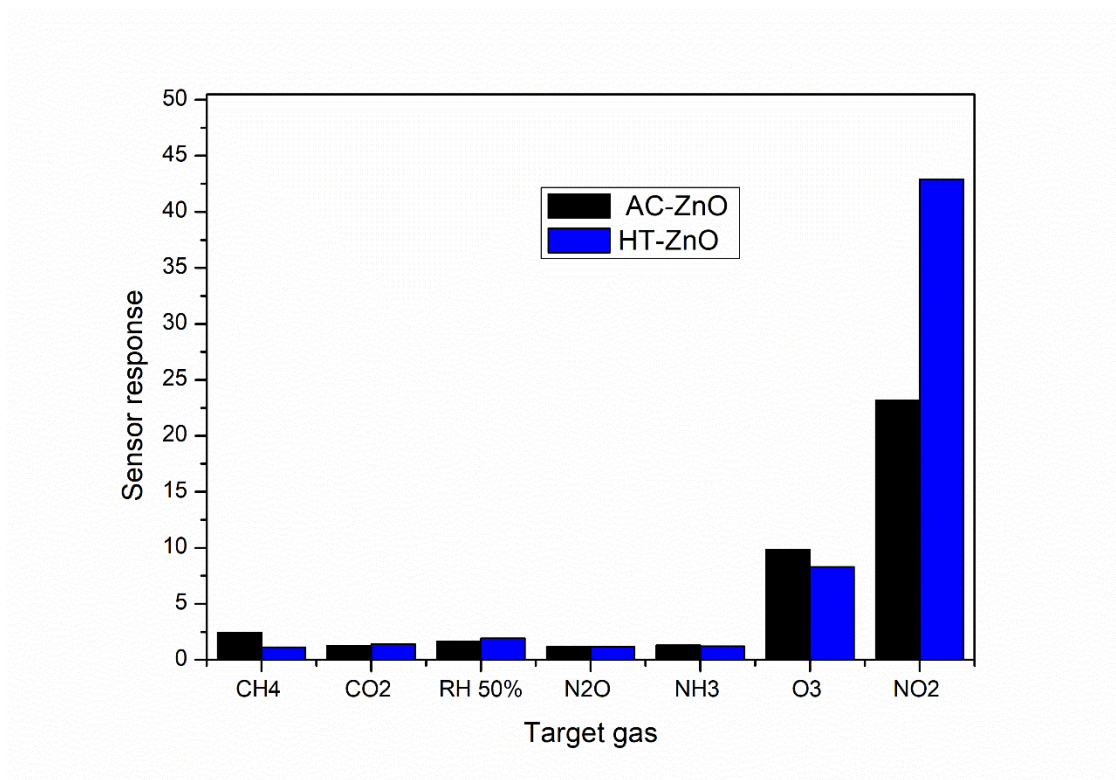

Fig. 9 Cross-sensitivity test of AC-ZnO (black) and HT-ZnO (blue) sensors at 150 °C.

Generally, the HT-ZnO sensor exhibits an enhanced selectivity for nitrogen dioxide detection than the AC-ZnO one. In particular, the sensor's response toward O$_3$ and water vapor is comparable for both sensors, whereas HT-ZnO sensor's response is almost double for NO$_2$ 250 ppb with respect to AC-ZnO sensor.

Repeatability tests were performed by exposing the AC-ZnO and HT-ZnO sensors toward 250 ppb of NO$_2$ for 3 pulses and results are illustrated in figure 10.
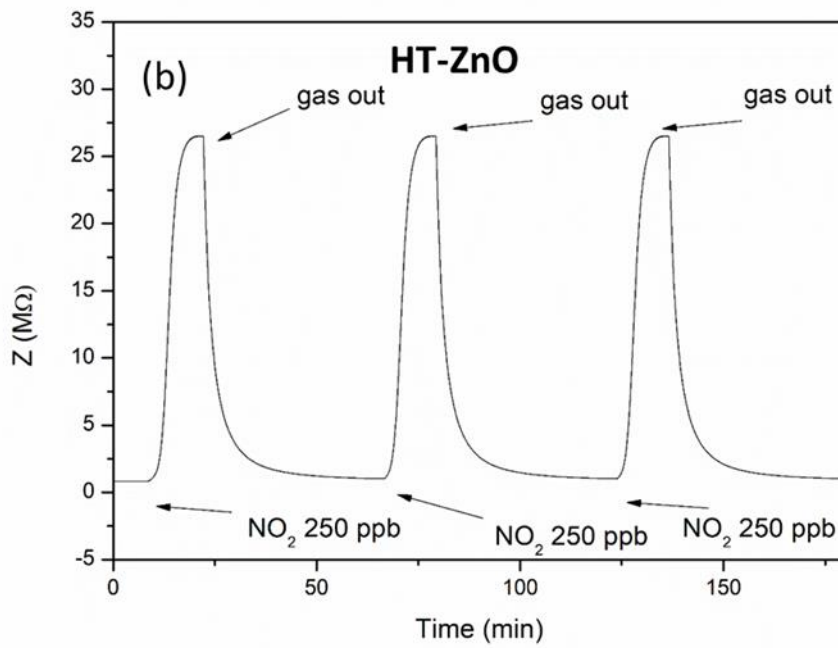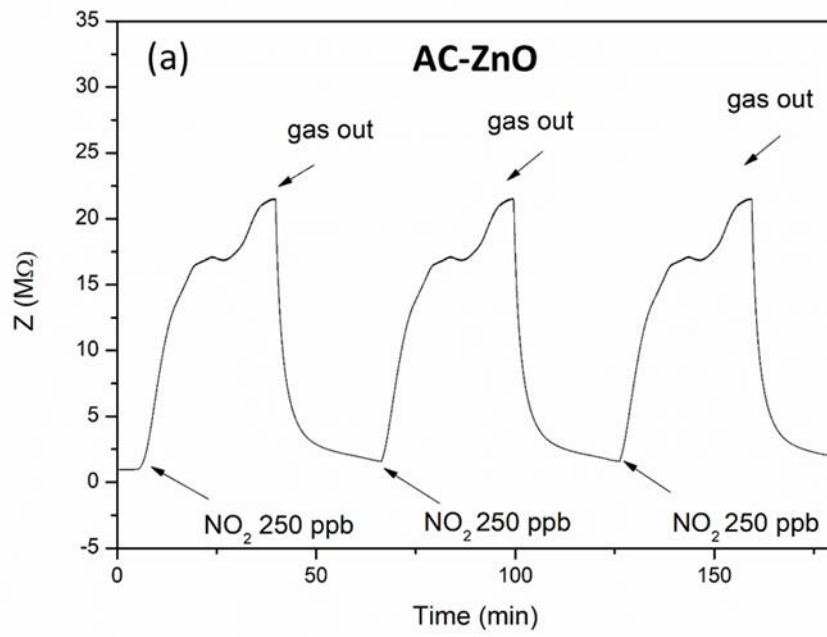
Fig. 10 Repeatability tests of AC-ZnO (a) and HT-ZnO (b) sensors toward 250 ppb of NO_2 in dry air at 150 °C.

Both sensors exhibit a great repeatability among different nitrogen dioxide 250 ppb exposures at the best operating temperature of 150 °C. Both sensors display the same sensor response, response and recovery times of the previous tests.

Despite only few studies have investigated the sensitivity of ZnO films toward NO_2 at low temperature so far, in Table 3 the current results are compared to such previous studies.

Table 3. Comparison of the NO_2 sensing performance of ZnO sensors working at low temperature.

Type of ZnO	Synthesis method	[NO₂] (ppm)	Sensor response (R=Z_g/Z_0)	Operating temperature (°C)	Response time (s)	Recovery time (s)	Reference
Nanopetals	Chemical precipitation	20	119	25	85	103	[24]
Nanowalls	Solution route	5	6.54	25	23	11	[25]
PH3HT-ZnO (1:1)	Spin coating	50	1.8	25	n.d.	n.d.	[26]
Nanorods	Hydrothermal	0.1	1.24	100	n.d.	n.d.	[40]
ZnO film	Successive ion layer adsorption and reaction (SILAR)	10	1.01	150	n.d.	n.d.	[41]
ZnO glass-ceramic	Melt-quenching	1	17	150	310	n.d.	[42]
Desert rose	Hydrothermal	0.25	31.51	150	341	451	This work
Rectangular-romboedric shape	Sol-gel autocombustion	0.25	21.67	150	652	788	This work

NB: n.d. = not determined. PH3HT: poly(3-hexylthiophene).

Comparing the present work with the state of the art regarding low-temperature ZnO sensors for NO_2, AC-ZnO and HT-ZnO sensors' response and recovery time are longer, even though a noticeable increase in the sensor response at sub-ppm level was attained. However, sensor response and recovery times in [25, 26] were determined while the sensor response was not completely stabilized.

The optimum operating temperature is on the boundary between the molecular-oxygen region (below 150 °C) and the ionic species one (above 150 °C) [43]. These species form a depletion layer at the surface of AC-ZnO and HT-ZnO due to electrons trapping [44, 45].

The measured impedances' variations are caused by direct chemisorption process of NO_2 molecules without involving the reaction with oxygen species [46].

A known series of reactions leading to nitrates and nitrites formation is reported in [47]: in this process, NO_2 reacts firstly at the oxygen vacancy (forming nitrites, NO_2^-), and then it participates in the formation of nitrates (NO_3^-) after reaction with O_2^-.

Electrons from the conduction band of ZnO are trapped when surface species are formed, but not during the oxidation from nitrites to nitrates. After the formation of nitrates, a further equilibrium is reached for the dissociation of nitrates to NO. Since the impedance and resistance increased upon exposure to 50-500 ppb of NO_2, the detection mechanism can be associated with the as-described reactions.

It is known from the literature [48,49] that the electrical resistance is strongly dependent on interfacial effects, grain boundaries and inter-particle contacts. As a consequence, sensor performances toward NO_2 at sub-ppm level of the nanostructures may be significantly influenced by the size, morphology and surface atomic structures of the gas sensing materials.

In the case of ZnO, porous structures display an increased number of surface-active sites compared to other forms of ZnO that can promote gas diffusion and mass transport processes and may therefore improve gas sensing properties [50].

Sensors based on ZnO that are presented in this work demonstrated that flower-like ZnO porous structures display superior gas sensing performance toward NO_2 compared to nanoparticle-type obtained by auto-combustion sol gel route. NO_2 interacts with a limited number of active sites on the ZnO surfaces, whose number is increasing in the case of the more porous samples; the HT-ZnO sensor possesses the greater proportion of high energy exposed ZnO facets with a greater number of surface-active sites compared to AC-ZnO. The higher sensor response and kinetics of interaction of HT-ZnO with NO_2 might thus be a result of the particular flower-like structure with 2D nanoplates, the voids and interspaces existing among nanoplates promoting both NO_2 adsorption

and desorption. As previously described, the more porous structure of HT-ZnO provides a higher specific larger surface area with more reactive sites for gas adsorption. Furthermore, HT-ZnO layer displays narrower distribution of agglomerate sizes controlling efficiently the contacts between the different agglomerates as well as the thickness of plate-like crystallites [51, 52].

In the case of AC-ZnO sensor, the presence of bigger agglomerates formed by smaller crystallites tends to reduce the gas permeability through the ZnO matrix especially at concentrations higher than 250 ppb.

By the results above reported it appears evident that the shape of ZnO particles is a key factor in determining the sensitivity and the response and recovery times of the sensors toward NO_2.

To conclude, the HT-ZnO sensors display higher degree of uniformity in terms of size, shape and surface structure that is beneficial in the interaction with nitrogen dioxide.

4   Conclusions

In this work, two different ZnO nano-powders were synthetized: one by an auto-combustion sol-gel route, and the other one by a hydrothermal process, resulting in ZnO flower-like nanostructures with enhanced specific surface area and lower degree of agglomeration with respect to the auto-combustion powder. Both ZnO sensing materials were obtained by simple, reproducible and low-cost processes, thus obtaining wurtzite-like crystalline structures as evidenced by detailed morphological characterization. Then, ZnO thick-film sensors were successfully fabricated for nitrogen dioxide detection at low temperature by screen-printing the sensing materials onto α-alumina substrates with platinum interdigitated electrodes and subsequently firing at 500 °C for 1 h in air.

The sensing properties toward NO_2 were studied for two ZnO nanostructures and showed that the best results were obtained at a relatively low temperature, i.e. 150 °C. In HT-sensors, the increase of specific surface area and the decrease of the degree of agglomeration of the nano-powder led to a more than double sensor response toward 250 ppb of NO_2 at 150 °C with respect to AC-ZnO sensor. Both sensors were almost insensitive to methane, ammonia, nitrous oxide, carbon dioxide and humidity. Only limited interferences with ozone were observed for both sensors, and the AC-ZnO sensors' response and recovery times were reasonably fast. All these results pave the way toward the realistic exploitation of these sensors as NO_2 detectors at ppb level and low temperature.

References

[1] EPA Technical Bulletin, Nitrogen Oxides (NOx), Why and How They Are Controlled? https://www3.epa.gov/ttncatc1/dir1/fnoxdoc.pdf. Accessed 5 October 2019.

[2] World Health Organization, Regional Office for Europe, Copenhagen, Denmark, Nitrogen dioxide Chapter 12, Global update, 2005.

[3] European Environment Agency. Air quality in Europe – 2012 report. EEA report No. 4/2012, 2012.

[4] N.N. Hansel, P.N. Breysse, M.C. McCormack, E.C. Matsui, J. Curtin-Brosnan, D.L. Williams, J.L. Moore, J.L. Cuhran, G.B. Diette, Environ. Health Perspect. 116, 1428 (2008).

[5] Air pollution in Europe 1990–2004, EU air quality directive 2001/81/CE.

[6] G. Korotcenkov, V. Brinzari, B.K. Cho, J. Sens. 2016, 3816094 (2016).

[7] Y. Ushio, M. Miyayama, H. Yanagida, Sens. Actuators, B 17, 221 (1994).

[8] E. Wiberg, N. Wiberg, A. F. Holleman, Inorganic Chemistry, 1st ed. (Academic Press, San Diego; De Gruyter, Berlin, 2001), p. 1884.

[9] Ü. Özgür, Y.I. Alivov, C. Liu, A. Teke, M. Reshchikov, S. Doğan, V. Avrutin, S.-J. Cho, H. Morkoç, J. Appl. Phys. 98 (2005) 041301.

[10] M. De Liedekerke, in Ullmann's Encyclopdia of Industrial Chemistry, Wiley-VCH, Weinheim, 2006.

[11] P. Rai, Y.-S. Kim, H.-M. Song, M.-K. Song, Y.-T. Yu, Sens. Actuators, B 165, 133 (2012).

[12] Z.L. Wang, ACS Nano 2, 1987 (2008).

[13] J. Zheng, Z.-Y. Jiang, Q. Kuang, Z.-X. Xie, R.-B. Huang, L.-S. Zheng, J. Solid State Chem. 182, 115 (2009).

[14] S. Kundu, U. Nithiyanantham, Ind. Eng. Chem. Res. 53, 13667 (2014).

[15] R. Sankar Ganesh, E. Durgadevi, M. Navaneethan, V.L. Patil, S. Ponnusamy, C. Muthamizhchelvan, S. Kawasaki, P.S. Patil, Y. Hayakawa, J. Alloys Compd. 721, 182 (2017).

[16] M. Das, D. Sarkar, Ceram. Int. 43, 11123 (2017).

[17] P. Patil, G. Gaikwad, D.R. Patil, J. Naik, Bull. Mater. Sci. 39, 655 (2016).

[18] L. Zhu, W. Zeng, Mater. Lett. 209, 244 (2017).

[19] L. Zhu, Y. Li, W. Zeng, Appl. Surf. Sci. 427, 281 (2018).

[20] X. Liu, J. Sun, X. Zhang, Sens. Actuators, B 211, 220 (2015).

[21] Z.S. Hosseini, A. Iraji zad, A. Mortezaali, Sens. Actuators, B 207, 865 (2015).

[22] L. Zhu, W. Zeng, Sens. Actuators, A 267, 242 (2017).

[23] T. Tesfamichael, C. Cetin, C. Piloto, M. Arita, J. Bell, Appl. Surf. Sci. 357, 728 (2015).

[24] R.K. Sonker, S.R. Sabhajeet, S. Singh, B.C. Yadav, Mater. Lett. 152, 189 (2015).

[25] L. Yu, F. Guo, S. Liu, B. Yang, Y. Jiang, L. Qi, X. Fan, J. Alloys Compd. 682, 352 (2016).

[26] J. Wang, X. Li, Y. Xia, S. Komarneni, H. Chen, J. Xu, L. Xiang, D. Xie, ACS Appl. Mater. Interfaces 8, 8600 (2016).

[27] A. Varma, A.S. Mukasyan, A.S. Rogachev, K.V. Manukyan, Chem. Rev. 116, 14493 (2016).

[28] W. Wen, J.-M. Wu, RSC Adv. 4, 58090 (2014).

[29] J.A. Conkling, C.J. Mocella, in Chemistry of Pyrotechnics: Basic Principles and Theory, CRC Press Taylor and Francis Group, Boca Raton, FL, USA, 2011, pp. 7–57.

[30] D. Pugliese, F. Bella, V. Cauda, A. Lamberti, A. Sacco, E. Tresso, S. Bianco, ACS Appl. Mater. Interfaces 5, 11288 (2013) .

[31] D. Ziegler, A. Marchisio, L. Montanaro, P. Palmero, J.-M. Tulliani, Solid State Ionics 320, 24 (2018).

[32] A. Khorsand Zak, W.H. Abd. Majid, M.R. Mahmoudian, M. Darroudi, R. Yousefi, Adv. Powder Technol. 24, 618 (2013).

[33] X. Zhang, W. Jiang, D. Song, H. Sun, Z. Sun, F. Li, J. Alloys Compd. 475, L34 (2009).

[34] Y. Tong, S. Zhao, X. Wang, L. Lu, J. Alloys Compd. 479, 746 (2009).

[35] K. Keis, E. Magnusson, H. Lindström, S.-E. Lindquist, A. Hagfeldt, Sol. Energy Mater. Sol. Cells 73, 51 (2002).

[36] C.M. Damaskinos, M.A. Vasiliades, V.N. Stathopoulos, A.M. Efstathiou, Catalysts 9, 621 (2019).

[37] V. Cauda, D. Pugliese, N. Garino, A. Sacco, S. Bianco, F. Bella, A. Lamberti, C. Gerbaldi, Energy 65, 639 (2014).

[38] G. Korotcenkov, V. Brinzari, B.K. Cho, Crit. Rev. Solid State Mater. Sci. 43, 83 (2017).

[39] A.D. McNaught, A. Wilkinson, in IUPAC. Compendium of Chemical Terminology, Gold Book Blackwell Scientific Publications, Oxford, 1997.

[40] S. Öztürk, N. Kilinç, Z.Z. Öztürk, J. Alloys Compd. 581, 196 (2013).

[41] V.L. Patil, S.A. Vanalakar, P.S. Patil, J.H. Kim, Sens. Actuators, B 239, 1185 (2017).

[42] M. Hassan, A.S. Afify, M. Ataalla, D. Milanese, J.-M. Tulliani, Sensors 17, 2538 (2017).

[43] N. Barsan, U. Weimar, J. Electroceram. 7, 143 (2001).

[44] X. Xue, Y. Nie, B. He, L. Xing, Y. Zhang, Z.L. Wang, Nanotechnology 24, 225501 (2013).

[45] P. Wang, Y. Fu, B. Yu, Y. Zhao, L. Xing, X. Xue, J. Mater. Chem. A 3, 3529 (2015).

[46] O. Berger, T. Hoffmann, W.-J. Fischer, V. Melev, Proc. SPIE 5116, Smart Sensors, Actuators, and MEMS, 24 April 2003.

[47] A. Chiorino, G. Ghiotti, F. Prinetto, M.C. Carotta, D. Gnani, G. Martinelli, Sens. Actuators, B 58, 338 (1999).

[48] N. Yamazoe, K. Shimanoe, J. Electrochem. Soc. 155, J93 (2008).

[49] K. J. Choi, H.W. Jang, Sensors 10, 4083 (2010).

[50] X. Wang, W. Liu, J. Liu, F. Wang, J. Kong, S. Qiu, C. He, L. Luan, ACS Appl. Mater. Interfaces 4, 817 (2012).

[51] J. Chang, M.Z. Ahmad, W. Wlodarski, E.R. Waclawik, Sensors 13, 8445 (2013).

[52] G. Korotcenkov, V. Macsanov, V. Tolstoy, V. Brinzari, J. Schwank, G. Faglia, Sens. Actuators, B 96, 602 (2003).

Abbreviations

AC-ZnO	HT-ZnO
Zinc oxide synthesized by auto-combustion sol-gel route	Zinc oxide synthesized by hydrothermal route